ChemCatChem

Research Article
doi.org/10.1002/cctc.202400343

Chemistry Europe
European Chemical Societies Publishing

www.chemcatchem.org

Efficient Alkaline Water Oxidation Electrocatalysis Enabled *via* the Modulation of Sn-Containing Anions towards NiFe Oxyhydroxide

Jiaxin Xu,[a] Ruotao Yang,[a] Tianjue Hou,[a] Jinxin Chen,[a] Hongyuan Yang,[b] Prashanth W. Menezes,*[b, c] and Ziliang Chen*[a, c]

Despite being considered as efficient non-noble metal-based electrocatalysts for alkaline oxygen evolution reaction (OER), NiFe (oxy)hydroxides ($NiFeO_xH_y$) typically fall short of meeting practical requirements. To address this challenge, herein, we introduce a facile *in situ* electrochemical incorporation technique to form Sn-doped NiFe-layered double hydroxide (NiFeSn-LDH) precatalysts. Subsequently, under the alkaline OER process, the precatalyst evolves into stannate ion-adsorbed NiFe oxyhydroxides (NiFeOOH). The presence of these stable stannate oxyanions plays a key role in mitigating Fe leaching, optimizing the electronic structure of NiFeOOH, and improving its reaction kinetics, thereby significantly enhancing alkaline OER performance. Notably, the nickel foam-supported NiFeSn-LDH demonstrates impressive results delivering a large current density of 100 mA cm^{-2} at an overpotential as low as ~260 mV and maintaining the industrial-relevant ~500 mA cm^{-2} current density over 5 days with negligible activity decay, surpassing the performances of most of the transition metal-based electrocatalysts. Comprehensive advanced characterizations of the precatalysts, before and after the OER reactions, have been performed to uncover stable residual stannate ions at the surface of $NiFeO_xH_y$ and to determine their pivotal role in promoting alkaline OER.

Introduction

Hydrogen energy is regarded as one of the most promising alternatives to conventional fossil fuels owing to its high energy density and notable environmental friendliness.[1–4] In contrast to traditional methods reliant on fossil fuels, water electrolysis offers a more efficient and eco-friendly means of generating H_2, and has garnered significant global research attention.[5–8] However, the development of water electrolysis is severely confined by its anodic half-reaction, *i.e.*, oxygen evolution reaction (OER), which suffers from sluggish reaction kinetics.[9,10] Recently, there has been a significant surge in the development of electrocatalysts aimed at boosting the performance of the OER.[11–14] Especially, current industrial alkaline OER catalysts predominantly comprise non-noble metals such as Ni and its alloys (e.g., Raney nickel), albeit exhibiting moderate catalytic performance.[15,16] Interestingly, over the past years, the nickel-iron systems, particularly NiFe(oxy)hydroxides ($NiFeO_xH_y$), emerged as the research focus in the field of OER, due to their inherent superior OER activity, as highlighted by notable contributions from the Bell and Boettcher groups.[17–19] Nevertheless, a key challenge with $NiFeO_xH_y$, lies in the dissolution of Fe atoms from its lattice into the electrolyte during alkaline OER especially under strengthened conditions (such as higher operating temperatures, pH levels, and extended operation periods), leading to significantly decreased performance and limiting their practical application potentials.[18,20,21] Therefore, there is a critical need to devise an effective, feasible, and straightforward method for stabilizing the Fe atoms within $NiFeO_xH_y$, thereby augmenting its intrinsic OER activity

On the other hand, currently, it is widely accepted that for most NiFe-based compounds including oxides, hydroxides, alloys, phosphides, borides, and chalcogenides,[22–27] it is inevitable that they undergo reconstruction into higher-valent $NiFeO_xH_y$ structures, that usually serves as the real active structures for alkaline OER. At the same time, other anions present in these precatalysts typically oxidize into water-soluble oxyanions, subsequently dissolving into the surrounding alkaline aqueous media (KOH or NaOH solutions).[28,29] The leaching of nonmetal species (such as S, Se, and P) is believed to significantly promote the formation of more porous surface structures, increasing the specific surface area, and accelerating

[a] J. Xu, R. Yang, T. Hou, J. Chen, Dr. Z. Chen
Institute of Functional Nano and Soft Materials (FUNSOM)
Jiangsu Key Laboratory for Carbon-Based Functional Materials and Devices
Soochow University
215123 Suzhou, P. R. China
E-mail: zlchen@suda.edu.cn

[b] H. Yang, Dr. P. W. Menezes
Department of Chemistry: Metalorganics and Inorganic Materials
Technische Universität Berlin
Straße des 17 Juni 135, Sekr. C2, 10623 Berlin, Germany
E-mail: prashanth.menezes@mailbox.tu-berlin.de

[c] Dr. P. W. Menezes, Dr. Z. Chen
Materials Chemistry Group for Thin Film Catalysis – CatLab
Helmholtz-Zentrum Berlin für Materialien und Energie
Albert-Einstein-Str. 15, 12489 Berlin, Germany
E-mail: prashanth.menezes@helmholtz-berlin.de

Supporting information for this article is available on the WWW under https://doi.org/10.1002/cctc.202400343

the OER capability of the in-situ reconstructed real active (oxy)hydroxides.[30,31] Furthermore, a couple of pioneering investigations have uncovered a fascinating phenomenon concerning transition metal (TM)-based precatalysts in alkaline OER. It has been observed that non-metal species, corroded into oxyanions, can undergo partial re-adsorption onto the surface of reconstructed TM-based (oxy)hydroxides (TMO_xH_y). This re-adsorption process further enhances the OER performance by optimizing the electronic structure of the associated TMO_xH_y, as well as its reaction kinetics and thermodynamics towards alkaline OER intermediates.[32–35] Similarly, gathering insights from Pourbaix diagrams of individual elements, it is theoretically conceivable that analogous oxygenation-dissolution-re-adsorption phenomena may occur with numerous metal species (such as Sn, Ge, Ti, and W) in TM-based precatalysts.[36] The reconstructed structures, i.e., the adsorption of metal-formed oxyanions onto the surface of TMO_xH_y, likely exhibit enhanced catalytic performance. However, investigations addressing this aspect are notably sparse, resulting in a significant gap in understanding the potential role of oxyanions in enhancing alkaline OER.

Taking the aforementioned concerns into consideration, stabilizing the metal-formed oxyanions adsorbed by $NiFeO_xH_y$ could offer a solution to addressing the challenge of unsatisfactory alkaline OER performance of $NiFeO_xH_y$, especially under industrial-relevant environments. Therefore, this study focuses on the deliberate development of a well-defined precatalyst for alkaline OER, Sn-doped NiFe-layered double hydroxide (NiFeSn-LDH), by a facile one-step electrodeposition process. This approach aims to achieve in-situ formation of the targeted NiFe oxyhydroxides (NiFeOOH) adsorbing stannate ions. This is because: firstly, NiFe-LDH materials are widely used as an effective OER precatalyst, which is known to readily transform into the higher-valent $NiFeO_xH_y$ during the alkaline water oxidation process;[37,38] Secondly, the Pourbaix diagram of Sn indicates that within the anodic OER potential window in 1 M KOH aqueous solution, Sn tends exist as $Sn(OH)_6^{2-}$, which is theoretically water-soluble.[36] As a result, a series of advanced characterizations supported this notion, revealing that after subjecting NiFeSn-LDH precatalyst to OER chronoamperometry (CP) for 24 h in 1 M KOH aqueous solution, the real active structure, i.e., $Sn(OH)_6^{2-}$ adsorbed NiFeOOH, is emerged. Notably, as expected, compared with the reference sample without the presence of Sn, the optimum NiFeSn-LDH supported on the fluorine-doped tin oxide (NiFeSn-LDH/FTO) glass substrate and nickel foam (NiFeSn-LDH/NF) exhibited significantly enhanced OER performances in 1 M KOH aqueous electrolyte. Specifically, NiFeSn-LDH/NF achieved a remarkable current density of as large as 100 mA cm^{-2} at an overpotential of only ~260 mV and maintained an industrial-relevant current density of 500 mA cm^{-2} over 5 days with minimal activity degradation, positioning it among the top-performing TM-based alkaline OER catalysts reported to date. This substantial performance enhancement can be attributed to the presence of adsorbed $Sn(OH)_6^{2-}$, which effectively shields the Fe atoms from leaching into the electrolyte, and modulates the electronic structure of NiFeOOH, thereby promoting its reaction kinetics. We believe the current work can inspire the community to stimulate further research efforts towards developing more efficient metal-formed oxyanions-incorporated non-noble metal-based OER electrocatalysts, and potentially extending such catalyst systems to other electrooxidation catalysis applications.

Results and Discussion

Synthesis of FTO-Supported NiFeSn-LDH and NiFe-LDH

To prepare the binder-free FTO-supported NiFeSn-LDH and NiFe-LDH, a typical three-electrode system was employed, where the FTO glass substrate, Pt foil, and saturated calomel electrode (SCE) served as the working, counter, and reference electrode, respectively. The aqueous electrolyte contained Ni^{2+}, Fe^{3+}, and Sn^{4+} with a targeted molar ratio. After exerting one-pot electrodeposition under a constant applied voltage of −1.2 V for 4 min, the NiFeSn-LDH and NiFe-LDH nanosheets were grown directly onto the surface of the FTO. Note that compared to the pristine NiFe-LDH with its characteristic hydrotalcite structure, the NiFeSn-LDH incorporates Sn into the double layers consisting of $[Ni_{1-x}Fe_xO_6]$ motifs (as illustrated in Figure 1 and Experimental Section).

Characterizations of NiFeSn-LDH and NiFe-LDH

The powder X-ray diffraction (PXRD) was first carried out on the as-prepared NiFeSn-LDH/FTO and NiFe-LDH/FTO, as well as the bare FTO substrate. In Figure 2a, apart from the peaks originating from the FTO, a low-crystallinity LDH phase can be observed, which is characteristically found for those LDH samples prepared using electrodeposition (PDF #40-0215).[39,40] In order to further explore the chemical state, phase composition, and morphology of NiFeSn-LDH and NiFe-LDH, X-ray photoelectron spectroscopy (XPS), Raman spectroscopy, field emission scanning electron microscopy (FESEM), as well as transmission electron microscopy (TEM) and the corresponding selected area electron diffraction (SAED), high-angle annular dark field-scanning transmission electron microscopy (HAADF-STEM) and the associated energy dispersive X-ray (EDX) characterizations were performed. In Figure S1a, the high-resolution Ni $2p_{3/2}$ XPS spectrum of NiFe-LDH can be fitted into a prominent peak at ~855.5 eV together with a minor peak at ~857.2 eV, indicative of Ni^{2+} and Ni^{3+}, respectively, characteristic of a typical NiFe-LDH structure.[41] Additionally, the Fe $2p_{3/2}$ XPS peak of NiFe-LDH was located at 712 eV, corresponding to the presence of Fe^{3+} (Figure S1b).[15,42] Notably, in the case of NiFeSn-LDH, both Ni 2p3/2 and Fe 2p3/2 displayed positive and negative shifts, respectively, indicating the successful incorporation of Sn atoms into the pristine NiFe-LDH lattice, which induced the electron interaction among host Ni and Fe atoms and their neighboring Sn dopants (Figure S1a, b).[15,43] Interestingly, an evident Sn $3d_{5/2}$ XPS signal representing Sn^{4+} was detected for NiFeSn-LDH at ~486.3 eV, further confirming the incorporation of Sn atoms[44] (Figure S1c). The Raman spectrum

Research Article
doi.org/10.1002/cctc.202400343
Chemistry Europe
European Chemical Societies Publishing

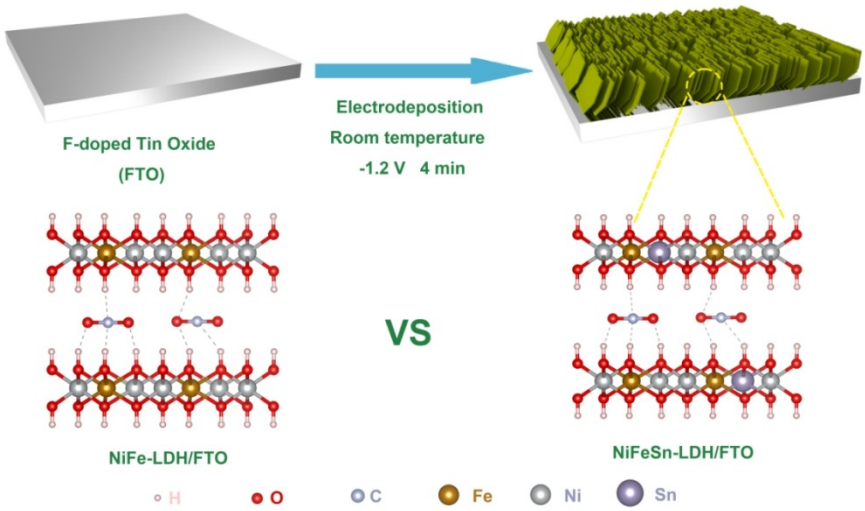

Figure 1. The schematic illustration for the synthesis of FTO-supported NiFeSn-LDH and NiFe-LDH.

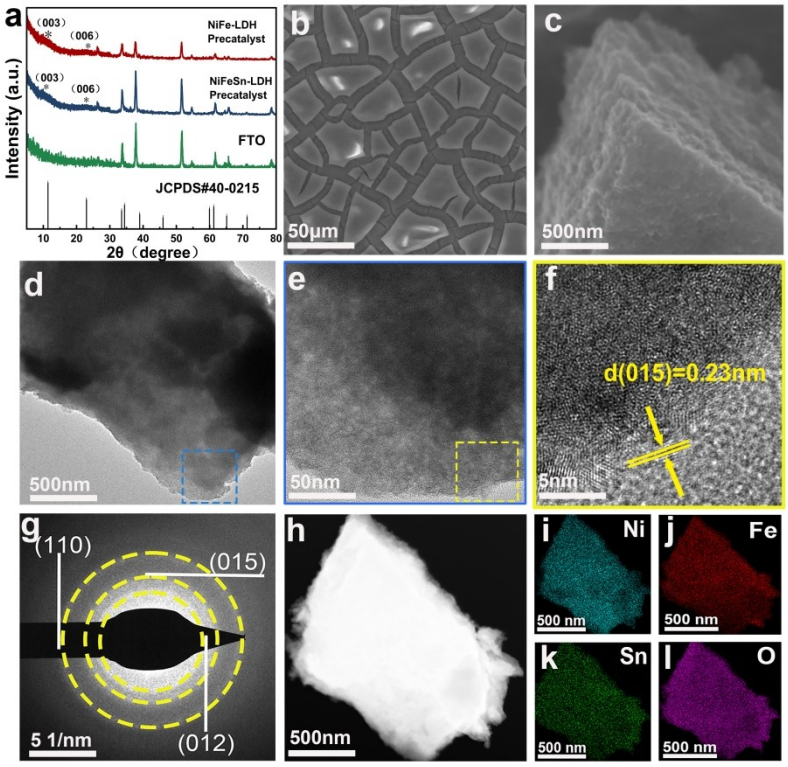

Figure 2. (a) The PXRD patterns of FTO, NiFe-LDH/FTO and NiFeSn-LDH/FTO, (b, c) The FESEM images of NiFeSn-LDH/FTO, (d, e) TEM image, (f) HRTEM image and (g) SAED pattern of NiFeSn-LDH/FTO, together with (h) corresponding HAADF pattern and elemental mappings of Ni (i), Fe (j), Sn (k), and O (l).

of NiFeSn-LDH depicted in Figure S2 exhibited two characteristic bands at ~457 and ~528 cm^{-1}, arising from the M^{3+}–O–M^{2+} and M^{3+}–O–M^{3+} in the LDH structure, implying successful preparation of our targeted catalyst.[45] The FESEM image of the as-prepared NiFeSn-LDH showed sheet-like nanostructures (Figure 2b, c), which can be affirmed by its TEM images (Figure 2d, e). The high-resolution TEM (HRTEM) image of NiFeSn-LDH presented discernible lattice fringes with a distance of 0.23 nm, indexed to the (015) plane of the LDH structure (Figure 2f). Moreover, the corresponding SAED pattern also signified the presence of (012), (015), and (110) facets of the LDH phase, further confirming the successful synthesis of the targeted material (Figure 2g). Besides, the HAADF-STEM pattern of such a sample with the associated EDX elemental

mapping images was also recorded (Figure 2h–l). The homogenous distribution of Ni, Fe, Sn, and O within the selected sample region demonstrated the expected doping of Sn into NiFe-LDH, which was also substantiated by the atomic ratio based on such EDX measurements (Ni:Fe:Sn = 1:0.26:0.02, Table S1). On the other hand, similar FESEM, TEM, HRTEM, and SAED results can be observed for the Sn-free NiFe-LDH sample (Figure S3a–g), also illustrating the successful formation of the LDH structure. Of note, the findings of the HAADF-STEM with the corresponding EDX revealed an even distribution of Ni, Fe, and O within the NiFe-LDH region, with an atomic ratio of Ni and Fe closely matching that of NiFeSn-LDH (Figure S3h–k and Table S2), This suggested that, in addition to the absence of Sn, NiFe-LDH possessed a morphology, phase structure, crystallinity, lattice parameters, and Ni/Fe content similar to those of NiFeSn-LDH. Despite these similarities, distinct differences in electrochemical OER performances between the two samples were observed under identical testing conditions, suggesting that the presence of Sn species could be the most prominent factor influencing the observed differences, which will be elaborated in the subsequent sections.

Electrocatalytic OER Performances

The OER performance of all samples was assessed in a typical three-electrode system under ambient conditions, employing a 1 M KOH aqueous solution as the electrolyte. The working electrode comprised FTO-supported samples, while a Hg/HgO electrode and Pt foil served as the reference and counter electrodes, respectively. To begin, we systematically screened the NiFeSn-LDH samples with varying Sn incorporation levels by electrodeposition in solutions containing progressively increased Sn proportions (relative to the total Ni^{2+}, Fe^{3+}, and Sn^{4+} concentrations in equimolar solutions), ranging from 0.05 to 0.15. In Figure S4, the SEM-EDS proved that the above proportion of the sample after deposition is strictly in accordance with the designed ratio. As shown in Figure S5, the fresh samples appear uniform color of yellow, and they turn to black after activation. The linear sweep voltammetry (LSV) results in Figure S6 unveiled that the NiFeSn-LDH with a Sn proportion of 0.1 exhibited the most favorable OER activity. Therefore, this sample was then selected for comprehensive characterization in the subsequent analyses. Next, we compared the OER electrochemistry of such an optimum NiFeSn-LDH deposited on FTO with the pristine NiFe-LDH/FTO. As illustrated in Figure 3a and Figure S7, NiFeSn-LDH/FTO demonstrated superior OER activity, i.e., affording 10 mA cm^{-2} current density at only ~252 mV overpotential, outperforming NiFe-LDH/FTO. Note that the bare FTO substrate showed inert OER activity and Figure S8 clearly ruled out the possible influence of Pt foil (counter electrode) for OER catalysis.[22] Figure S9 verifies the good reproducibility of the experiment by testing the LSV curves of three distinct electrodes. Subsequently, the Tafel analysis was measured by the steady-state method on both NiFeSn-LDH/FTO and NiFe-LDH/FTO.[46] As shown in Figure 3b, the former exhibited a significantly lower Tafel value, meaning more favorable reaction kinetics than the latter.[15,47] In addition, the cyclic voltammetry (CV) curves of NiFeSn-LDH/FTO and NiFe-LDH/FTO at different scanning rates were conducted to obtain their electrochemical double-layer capacitance (C_{dl}) values (Figures S10 and 3c). NiFeSn-LDH/FTO demonstrated a C_{dl} value of 0.1923 mF cm^{-2}, approximately double that of NiFe-LDH/FTO (0.1099 mF cm^{-2}). Given the fact that C_{dl} is proportional to the electrochemically active surface area (ECSA), this indicated that the incorporation of Sn species into NiFe LDH leads to an increase in surface active sites.

As there are no precise methods proposed for calculating accurate C_{dl} so far, we adopted the common determination of C_{dl} through CV cycling for calculation in the current work.[16,48] Furthermore, we normalized the LSV curves of NiFeSn-LDH/FTO and NiFe-LDH/FTO against their respective C_{dl} to understand their intrinsic activity.[32,49,50] Notably, Sn-doped NiFe-LDH displayed superior inherent activity compared to its Sn-free counterpart (Figure S11). Besides, the electrochemical impedance spectra (EIS) results manifested that Sn-doping can also boost the charge transfer ability during the OER process, which further contributed to the elevation of OER activity of NiFeSn-LDH (Figure 3d and Table S3). The stability tests for NiFeSn-LDH/FTO and NiFe-LDH/FTO were operated by chronopotentiometry (CP) measurement at a current density of 10 mA cm^{-2} for 24 h. In Figure 3e, only a slight activity decay was observed for NiFeSn-LDH/FTO, while the continuously increased overpotential for NiFe-LDH/FTO, indicating that the introduction of Sn dopants indeed improved the presented OER stability. Encouraged by the superior OER performances of NiFeSn-LDH/FTO, we also electrodeposited NiFeSn-LDH on nickel foam (NiFeSn-LDH/NF) substrate with excellent electrical conductivity and three-dimensional macroporous architecture. The FESEM images first confirmed the homogenous growth of NiFeSn-LDH on NF (Figure S12a–c). Meantime, the TEM, HRTEM, SAED, and HAADF-STEM with EDX characterizations on the NiFeSn-LDH peeled from NF demonstrated that NF-supported NiFeSn-LDH had a similar morphology, phase structure, crystallinity, and lattice parameters to those deposited on FTO (Figure S12d–l). Based on these points, we conducted the OER electrochemistry towards NiFeSn-LDH/NF with the reference sample, NiFe-LDH deposited on NF (NiFe-LDH/NF) using the same method and conditions. As expected, the LSV (Figure 3f), Tafel slope (Figure S13), C_{dl} (Figure S14a–c) and the associated C_{dl}-normalized LSV (Figure S14d), as well as EIS (Figure 3g and Table S4) results uncovered the similar trend between NiFeSn-LDH/NF and NiFe-LDH/NF to the cases when deposited on FTO. Notably, NiFeSn-LDH/NF only required an overpotential of as low as ~260 mV to deliver 100 mA cm^{-2} current density, and its Tafel slope was merely ~38.78 mV dec^{-1} (Figure 3f). It is worth noting that such an alkaline OER activity of NiFeSn-LDH/NF surpassed previously documented TM-based catalysts supported on NF (Figure 3h and Table S5). Subsequently, to measure how much oxygen is experimentally observed relative to the amount that is theoretically predicted, the faraday efficiency (FE) was measured. In Figure S15, the highest OER FE of NiFeSn-LDH/FTO was determined as 97%, which shows that NiFeSn-LDH/NF has a good efficiency in the electrolytic process.[51] Eventually, the

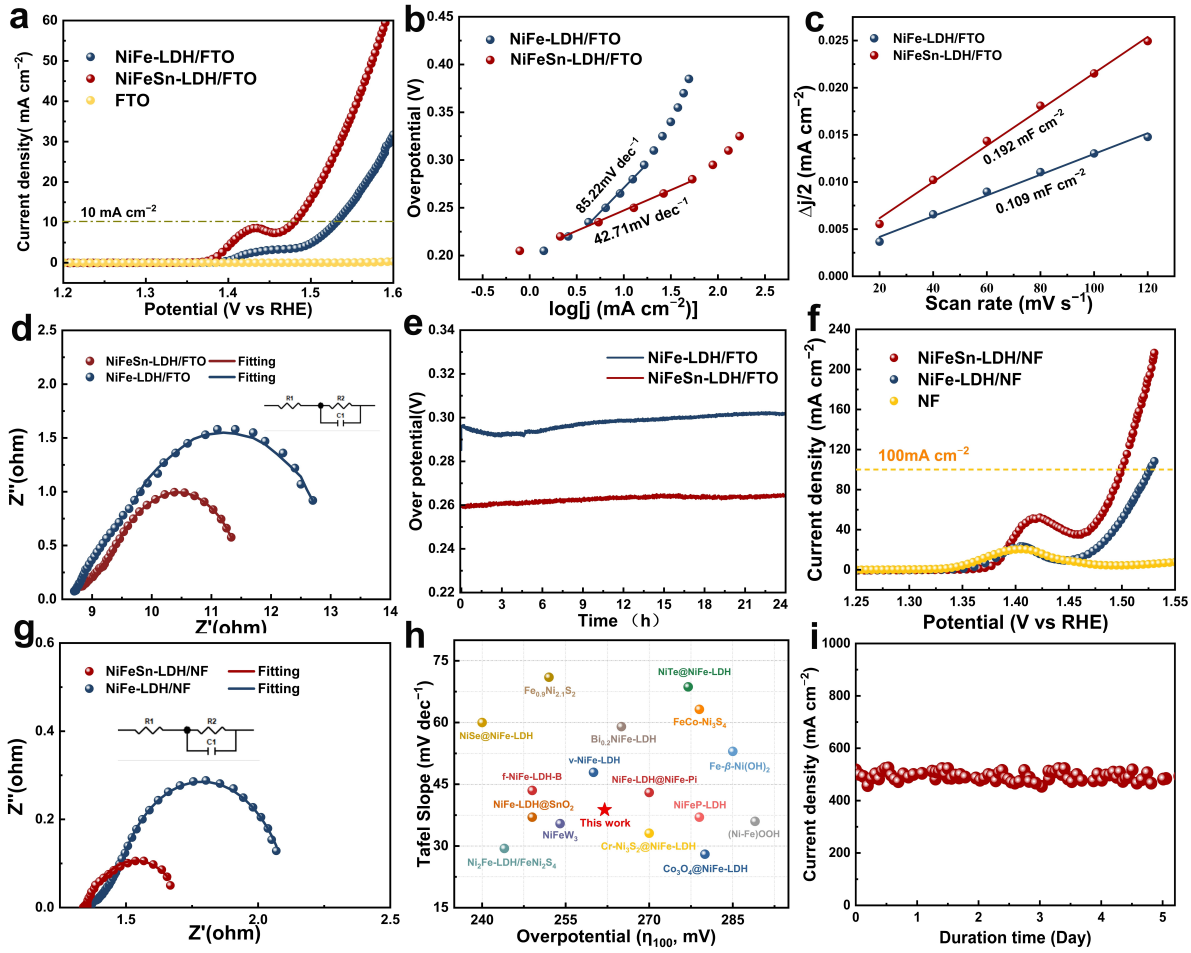

Figure 3. (a) Comparison of linear sweep voltammetry curves of NiFe-LDH/FTO and NiFeSn-LDH/FTO at the scanning rate of 5 mV s^{-1}. (b) The Tafel curves of NiFe-LDH/FTO and NiFeSn-LDH/FTO under steady-state conditions. (c) The C_{dl} value of NiFe-LDH/FTO and NiFeSn-LDH/FTO achieved by acquiring CV curves at scanning rates of 20, 40, 60, 80, 100, and 120 mV s^{-1}, followed by calculations. (d) Nyquist plot of NiFe-LDH/FTO and NiFeSn-LDH/FTO obtained from EIS fitting to an equivalent circuit at an anodic potential of 1.53 V (vs RHE). (e) The stability test curve acquired by conducting CP tests on NiFe-LDH/FTO and NiFeSn-LDH/FTO at a current density of 10 mA cm^{-2}. (f) Linear sweep voltammetry curves of NiFe-LDH/NF, NiFeSn-LDH/NF, and NF at the scanning rate of 5 mV s^{-1}. (g) Nyquist plot of NiFe-LDH/NF and NiFeSn-LDH/NF attained from EIS fitting to an equivalent circuit at an anodic potential of 1.5 V (vs RHE). (h) The performance comparison using overpotentials and Tafel slopes of the current NiFe-based catalysts in alkaline environments. (i) The observed stability curve by conducting a CA test lasting over 5 days at a current density of 500 mA cm^{-2}.

practical application potential of our NiFeSn-LDH/NF was assessed,(Figure 3i). Under a chronoamperometry (CA) at an industrial-relevant current density of ~500 mA cm^{-2}, the NiFeSn-LDH/NF maintains a remarkable stability curve over 5 days, affirming its promising prospects for further larger-scale application.

Determination of the Active Structures and Role of the Doped Sn

As aforementioned, it is widely accepted that the surface reconstruction of NiFe-LDH would inevitably occur during the OER process in alkaline media. Therefore, to understand the real active structures of the investigated catalysts in the present work, as well as the role of the doped Sn in promoting the basic OER performances, herein, a series of post-OER (after 24 h OER CP at 10 mA cm^{-2}) characterizations were carried out based on the samples supported on FTO (to exclude possible interferences from the NF substrate).

To begin, comparing their initial states, the PXRD pattern of post-OER NiFeSn-LDH/FTO and NiFe-LDH/FTO showed that in addition to the peaks originating from the FTO substrate, very similar weak and broad (003) and (006) peaks assigned to LDH phase were hardly be identifiable (Figure 4a). This observation suggests the structural transformation of NiFeSn-LDH to NiFe-based oxyhydroxides. To gain more insights into this point, surface-sensitive techniques including Raman and XPS spectroscopies were adopted on the samples peeled from the FTO substrate. As displayed in Figure 4b, two characteristic bands, *i.e.*, E_g bending and A_{1g} stretching vibration of Ni–O in NiOOH were easily discernible in the Raman spectra of the post-OER NiFeSn-LDH (at ~480 and ~565 cm^{-1}) and NiFe-LDH (at ~473 and ~560 cm^{-1}).[15,52,53] These findings manifested that these two LDH precatalysts successfully transformed into the NiFe oxyhydroxides (NiFeOOH).[15] Notably, two points are worth

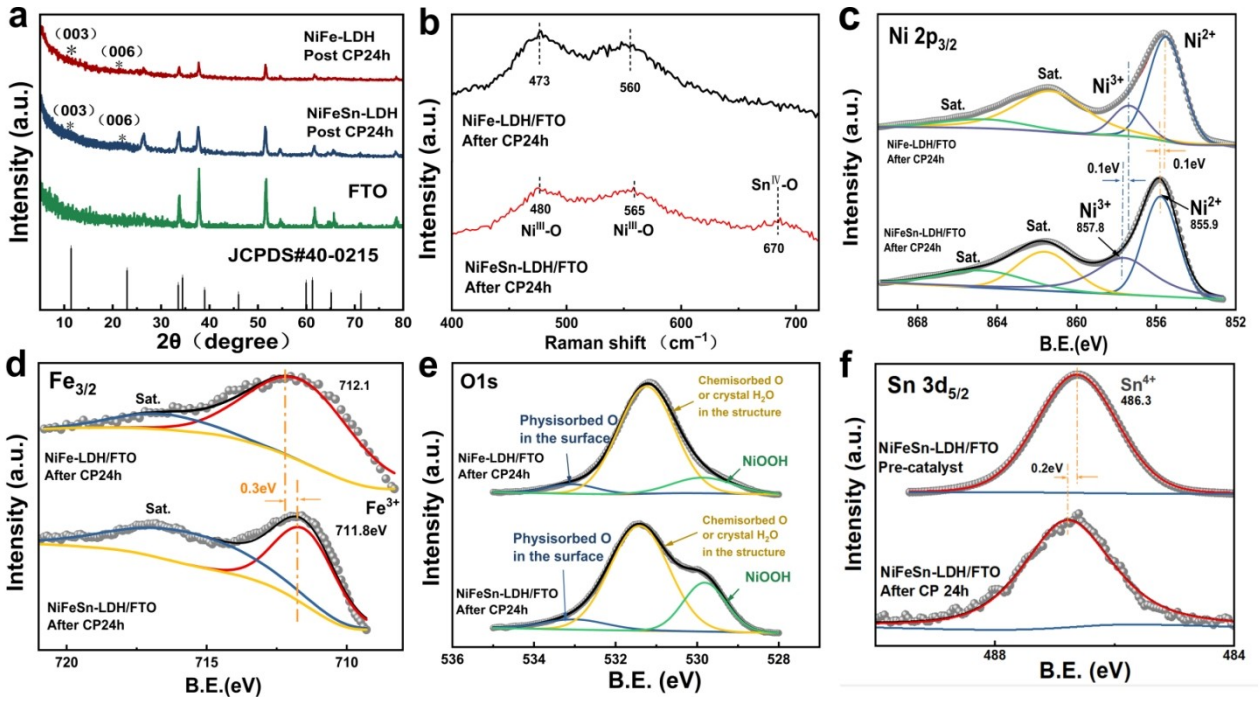

Figure 4. (a) XRD patterns of NiFe-LDH/FTO and NiFeSn-LDH/FTO after CP test. (b) Raman spectra of NiFe-LDH/FTO and NiFeSn-LDH/FTO after CP test. The high resolution (c) Ni $2p_{3/2}$, (d) Fe $2p_{3/2}$ and (e) O 1s XPS spectra of NiFe-LDH/FTO and NiFeSn-LDH/FTO after CP test. (f) High resolution Sn $3d_{5/2}$ XPS spectra of NiFeSn-LDH/FTO before OER and after CP test.

mentioning: i) In the case of post-OER NiFeSn-LDH, an additional band was clearly identified at ~670 cm^{-1}, originating from the presence of the Sn^{4+}–O bond.[54] Intriguingly, such a band was absent in the spectrum of the same NiFeSn-LDH sample before electrochemistry. This can be probably interpreted that the Sn dopants within the NiFe-LDH lattice were evolved as water-soluble $Sn(OH)_6^{2-}$ during the OER process in 1 M KOH aqueous solution (as predicted by the Pourbaix diagram of Sn).[36] As demonstrated by considerable previous works, the anions of many TM-based compounds would transform into oxyanions during alkaline OER, which were dissolved into the aqueous electrolytes and subsequently re-adsorbed by the concurrently *in-situ* reconstructed TM-based (oxy)hydroxides. Accordingly, in the case of NiFeSn-LDH, the dissolved $Sn(OH)_6^{2-}$ was then re-adsorbed by the surface of *in-situ* evolved NiFeOOH; ii) In the system of NiFeOOH, the Raman intensity ratio of E_g bending and A_{1g} stretching vibration of Ni–O (I_{Eg}/I_{A1g}) can serve as a direct indicator of amounts of Fe dopants within NiOOH. Typically, the lower this intensity ratio, the more Fe is present.[15,55] The I_{Eg}/I_{A1g} value of the post-OER NiFeSn-LDH (0.175) was apparently lower than that of the post-OER NiFe-LDH (2.812), indicating more stabilized Fe. This could be attributed to the presence of surface-adsorbed $Sn(OH)_6^{2-}$ may inhibit the leaching of Fe from the reconstructed NiFeOOH during the OER process.

Additionally, the XPS results of Ni $2p_{3/2}$ XPS for both post-OER NiFeSn-LDH and post-OER NiFe-LDH revealed an evident increase in the proportion of Ni^{3+} compared to Ni^{2+}, signifying the surface reconstruction of LDH into higher-valence oxyhydroxide (Figure 4c). In the Fe $2p_{3/2}$ XPS spectra for both samples, the Fe^{3+} peaks positively shifted compared with those in their respective spectra before electrochemistry, also substantiating the occurrence of surface oxidative reconstruction (Figure 4d). Moreover, the surface evolution of oxyhydroxides can be further verified by the O 1s XPS spectra of these two samples (Figure 4e), from which NiOOH could be identified.[56,57]

Furthermore, the Sn $3d_{5/2}$ XPS peak indicative of Sn^{4+} slightly shifted to higher binding energy for the post-OER NiFeSn-LDH compared with that for the sample before OER. This demonstrated that the doped Sn^{4+} within the NiFe-LDH was evolved as a stannate ion and then adsorbed on the surface of reconstructed NiFeOOH during OER in 1 M KOH aqueous solution, in agreement with the Raman data and analysis (Figure 4f). Another noteworthy point here is that the XPS peaks representing Ni^{3+} and Ni^{2+}, as well as Fe^{3+} for the post-OER NiFeSn-LDH emerged at higher and lower binding energy positions, respectively, compared with those for the post-OER NiFe-LDH, unveiling the electronic modification of the reconstructed NiFeOOH induced by its surface-adsorbed stannate ions (Figure 4c, d). On the other hand, various microscopic characterizations were also employed to determine the real active structures of NiFeSn-LDH and NiFe-LDH under alkaline water oxidation. The FESEM images of post-OER NiFeSn-LDH and post-OER NiFe-LDH both displayed sheet-like morphology, which are the typical structures for (oxy)hydroxides[58,59] (Figures 5a, b and S16a, b). Such a morphology can be further proven through TEM images of these two samples (Figures 5c and S16c). In addition, from the HRTEM images in Figure 5d, the distance of the lattice fringes at the edge region of the post-OER NiFeSn-LDH can be identified as 0.206 nm, which can be

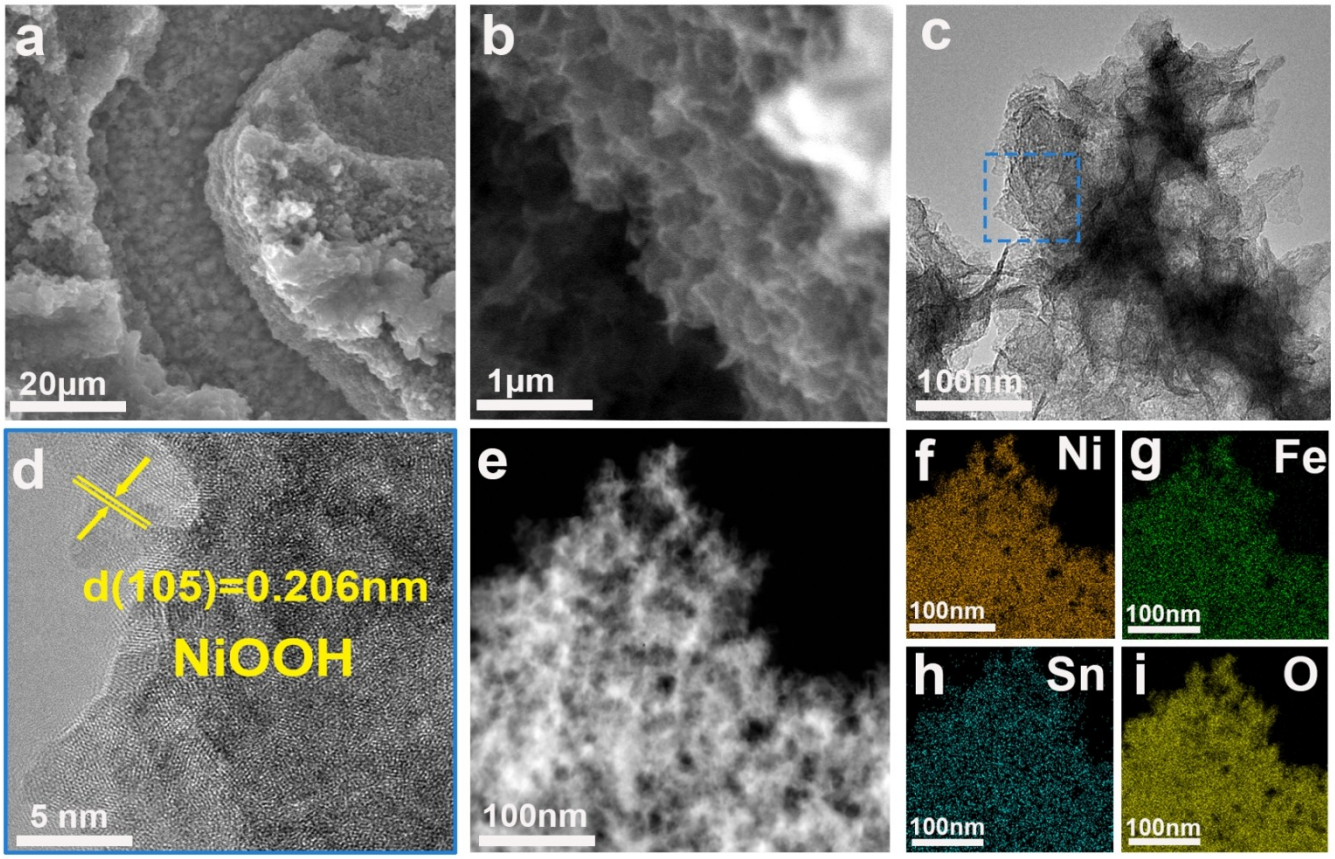

Figure 5. (a, b) FESEM images of NiFeSn-LDH/FTO after the CP test, (c) TEM image and (d) HRTEM image of NiOOH scratched off from NiFeSn-LDH/FTO after the CP test, together with (e) corresponding HAADF pattern and elemental mappings of Ni (f), Fe (g), Sn (h), and O (i).

ascribed to the (105) plane of NiOOH (PDF #6-75). Similarly, the (105) plane and (101) plane of NiOOH (PDF #6-75) can also be found from the HRTEM image against the edge of the post-OER NiFe-LDH (Figures S16d). Besides, from the HADDF-STEM pattern and the associated EDX elemental mapping, Ni, Fe, Sn, and O were distributed evenly within the selected post-OER NiFeSn-LDH area, implying the stable existence of $Sn(OH)_6^{2-}$ (as oxyanion) adsorbed on the surface of in-situ evolved NiFeOOH (Figure 5e–i). Analogically, homogenous Ni, Fe, and O can be also found in the region of post-OER NiFe-LDH (Figure S16e–h). Importantly, the corresponding EDX atomic ratio results showed that sufficient Sn was still retained for the post-OER NiFeSn-LDH, arising from the remained LDH precatalyst and the re-adsorbed $Sn(OH)_6^{2-}$.

In contrast, compared to the post-OER NiFe-LDH, substantially more Fe was found in the NiFeSn-LDH after OER CP (Tables S1, S2), consistent with the Raman analysis, *i.e.*, the presence of $Sn(OH)_6^{2-}$ could effectively protect the Fe within NiFeOOH from leaching into the KOH electrolyte during OER process. According to the Pourbaix diagram, it can be seen that Sn and Fe will form $Sn(OH)_6^{2-}$ and ferrate ions, respectively, which then dissolve into the electrolyte in a strong alkali environment.[36] Due to the high electronegativity of oxygen anion ($Sn(OH)_6^{2-}$), there is a strong interaction between Fe element and oxygen anions, which weakens the occupation between the 3d orbital of Fe^{3+} and the 1 s orbital of OH^- in the electrolyte, thus effectively avoiding the oxidation of Fe element to a higher valance state in a strong alkali environment.[60–63]

Based on the above post-OER characterizations, we can conclude that the surface of NiFeSn-LDH and NiFe-LDH reconstructed into the NiFeOOH with and without $Sn(OH)_6^{2-}$ adsorption, respectively. At the same time, the improved activity and stability of NiFe-LDH induced by Sn doping mainly stemmed from the re-adsorption of the $Sn(OH)_6^{2-}$ on the surface of the in-situ reconstructed NiFeOOH during the OER process, and the involved alkaline OER reaction steps are summarized in Figure S17.[11] The stable presence of the surface $Sn(OH)_6^{2-}$ can greatly suppress the dissolution of Fe from NiFeOOH during basic OER, as well as tune the electronic structure of NiFeOOH and enhance its reaction kinetics.[64,65]

Conclusions

In this study, we synthesized a Sn-doped NiFe-layered double hydroxide (NiFeSn-LDH) using a facile electrodeposition technique for alkaline OER. Based on the comprehensive pre- and

post-OER characterizations, coupled with the related background knowledge, we reasonably conclude that during water oxidation in 1 M KOH aqueous media, the Sn dopants from NiFeSn-LDH were evolved as the soluble $Sn(OH)_6^{2-}$, dissolved into the electrolyte, and are subsequently re-adsorbed onto the concurrently reconstructed NiFeOOH surface. This stable existence of surface-adsorbing oxyanions effectively prevented the leaching of Fe atoms from the NiFeOOH lattice. Furthermore, it induced beneficial alterations in the electronic structure of NiFeOOH, resulting in enhanced OER kinetics. Notably, when NiFeSn-LDH is deposited on the conductive NF, it can afford a current density of 100 mA cm^{-2} at an overpotential of only ~260 mV, as well as maintain an industrial-relevant current density of as high as ~500 mA cm^{-2} over 5 days without visible activity degradation. This performance surpasses that of most reported TM-based electrocatalysts for alkaline OER. Our work sheds light on the key role of residual surface oxyanions during water oxidation and provides insight into the design strategy to develop a new generation of low-cost, high-performance NiFe-based catalysts for water electrolysis. It is also intriguing to discover that the adsorption of residual surface Sn-containing oxyanions can positively influence the OER performance of d-block TM-based precatalysts as well as potentially improve the kinetics by stabilizing OER reaction intermediates.[31,33] This finding is likely to inspire further development of novel *p*-block metals (such as Ge, Bi, Al, and In)-mediated TM-based precatalysts for electrocatalysis.

Experimental Section

Chemicals and Materials

Deionized water was used to carry out all the experiments. The potassium hydroxide KOH (95%), nickel nitrate $Ni(NO_3)_2 \cdot 6H_2O$ (98%), ferrous nitrate $Fe(NO_3)_2 \cdot 9H_2O$ (98.5%) were acquired from Sinopharm Group Co. Ltd. and $SnCl_4 \cdot 4H_2O$ was obtained from Macklin Biochemical Technology Co., Ltd. The electrode substrates NF and FTO were purchased from Merck & Co., Inc.

Synthesis of NiFeSn-LDH and NiFe-LDH

The electrodeposition was conducted in a standard three-electrode system, where bare FTO or NF served as the working electrode, Pt foil worked as the counter electrode, and SCE was used as the reference electrode. Ni $(NO_3)_2 \cdot 6H_2O$, $Fe(NO_3)_3 \cdot 9H_2O$, and $SnCl_4 \cdot 4H_2O$ (totally 50 mM) were dissolved into 50 mL deionized water with a molar ratio of $Ni^{2+}:Fe^{3+}:Sn^{4+} = 4:1:0.56$ (the Sn^{4+} proportion relative to the total molar sum of Ni^{2+}, Fe^{3+}, and Sn^{4+} was ~0.1). For optimizing the Sn dopants, the electrodeposition was also performed in the aqueous solution where the proportion of Sn^{4+} against the total molar of Ni^{2+}, Fe^{3+}, and Sn^{4+} was ~0.05 and ~0.15 (note that the volume of the deposition solution and molar ratio of $Ni^{2+}:Fe^{3+}$ was fixed as 50 mL and 4:1, respectively). The constant applied potential was set as −1.2 V for 240 s with a CHi760e electrochemical workstation. The resulting loading mass was around ~1.03 mg cm^{-2} on the FTO, and that on NF was comparable. For the preparation of FTO or NF-supported NiFe-LDH preparation, the same procedure as mentioned above was followed, except no Sn^{4+} source was included. The loading mass was controlled to match that of the NiFeSn-LDH case.

Characterization

The phase information of the studied samples was obtained using PXRD on a Bruker D8 ADVANCE X-ray diffractometer with Cu Kα radiation (λ = 1.5406 Å). The morphology and structure of the targeted samples were investigated by FESEM (electron microscopy SU800, Hitachi, Tokyo, Japan) at a 20 kV acceleration. The TEM (FEI Talos F200X) was further employed to gain more insights into their microstructures, phase, as well as composition presence and distribution. The XPS measurements were carried out on an ESCALAB 250Xi spectrometer (Thermo Scientific, USA) equipped with a pass energy of 30 eV with a power of 100 W (10 kV and 10 mA) and a mono-chromatized α X-ray (hν = 1486.65 eV) source. All samples were analyzed under a pressure of less than 1.0×10^{-9} Pa. Spectra were acquired through the avantage software (Version 5.979) with a step of 0.05 eV. The Raman spectroscopy was recorded using a Horiba LabRam HR Evolution confocal Raman microscope with a laser excitation wavelength of 473 nm, laser power of 1.25 mW, and 100× objective lens (NA = 0.95).

Electrochemical Measurements

The electrochemistry was conducted using a CHi760e and EC-Lab electrochemical workstations in a standard three-electrode system. The catalysts electrodeposited on different substrates directly served as the working electrodes, while a Pt foil (1×1 cm) and Hg/HgO electrode acted as the counter electrode and reference electrode, respectively. The LSV, CV, CP, and CA experiments were carried out with an iR compensation of 95% on the CHi760e instrument. Moreover, the CV and LSV tests were conducted at a scan rate of 5 mV s^{-1}. All measured potentials were calibrated with respect to RHE based on the following equation: E(RHE) = E(Hg/HgO) + 0.098 V + (0.0591×pH) V, where the pH value of 1 M KOH was adopted from our previous report.[66] The method for calculating overpotential involves measuring the potential at a current density of 10 mA cm^{-2} and then subtracting the theoretical potential for water splitting ($\eta_{10} = E_{RHE} - 1.23$ V). The choice of 10 mA cm^{-2} as a reference point is because this current density is close to the practical operating conditions for solar fuel synthesis, thus holding significant practical value.[67] The Tafel slope, C_{dl}, and EIS were conducted on the EC-Lab electrochemical workstation. The Tafel slope was determined through a steady-state measurement, i.e., the CA was performed at a fixed potential for 3 minutes, and the applied potential gradually increased with an interval of 15 mV.[50] The average current density obtained at each potential was used for the calculation of Tafel plots. The Tafel slope was determined according to the Tafel equation: $\eta = b\log j + a$, where η, b, and j represent overpotential (V), Tafel slope (mV dec^{-1}), and current density (mA cm^{-2}), respectively. To assess the C_{dl}, CV was performed at a non-Faradaic voltage region. The half of the difference for the current density at the middle point of the CV potential window was plotted as a function of the scan rate, yielding the corresponding slope, which is the specific value of C_{dl}. The EIS was recorded at 1.53 V (vs. RHE) for catalysts deposited on FTO, as well as 1.50 (vs. RHE) for the ones on NF. The amplitude of the sinusoidal wave was determined in a frequency range of 100 kHz to 1 mHz. The charge transfer resistance (R_{ct}) was reflected by the diameter of the semicircle in the Nyquist plots after fitting in the EC-Lab. The FE was measured through the water drainage method. During this process, a consistent potential was maintained at the electrode, while the volume of gases (oxygen) generated was continuously tracked. Subsequently, the quantity of hydrogen moles was determined by utilizing gas laws. Lastly, the theoretically anticipated amount of O_2 was calculated by invoking the Faraday law, which asserts that the passage of 96,500 coulombs produces one equivalent of a chemical reaction.[51]

Acknowledgements

This work is supported by National Natural Science Foundation of China (52201269), Natural Science Foundation of Jiangsu Province (BK20210735), Collaborative Innovation Center of Suzhou Nano Science & Technology, the 111 Project, and Suzhou Key Laboratory of Functional Nano & Soft Materials and Jiangsu Key Laboratory for Advanced Negative Carbon Technologies. Z. C. gratefully acknowledges the funding from Gusu leading talent plan for scientific and technological innovation and entrepreneurship (ZXL2022487). H. Yang thanks China Scholarship Council (CSC) for the Ph.D. fellowship. P. W. M. greatly acknowledges support from the German Federal Ministry of Education and Research in the framework of the project Catlab (03EW0015A/B) and project PrometH2eus (03HY105C). Open Access funding enabled and organized by Projekt DEAL.

Conflict of Interests

The authors declare no conflict of interest.

Data Availability Statement

The data that support the findings of this study are available from the corresponding author upon reasonable request.

Keywords: electrochemical reconstruction · leaching-adsorption · oxyanions · NiFe (oxy)hydroxides · alkaline OER

[1] J. Song, C. Wei, Z.-F. Huang, C. Liu, L. Zeng, X. Wang, Z. J. Xu, *Chem. Soc. Rev.* **2020**, *49*, 2196–2214.
[2] R. A. Field, R. G. Derwent, *Int. J. Hydrogen Energy* **2021**, *46*, 30190–30203.
[3] M. Yu, E. Budiyanto, H. Tüysüz, *Angew. Chem. Int. Ed.* **2022**, *61*, e202103824.
[4] X. Jia, Y. Zhao, G. Chen, L. Shang, R. Shi, X. Kang, G. I. N. Waterhouse, L.-Z. Wu, C.-H. Tung, T. Zhang, *Adv. Energy Mater.* **2016**, *6*, 1502585.
[5] Shantharaja, Giddaerappa, V. A. Sajjan, K. S. Lokesh, *Int. J. Hydrogen Energy* **2023**, *48*, 35850–35861.
[6] S. Aralekallu, K. S. Lokesh, V. Singh, *Fuel* **2024**, *357*, 129753.
[7] T. Terlouw, C. Bauer, R. McKenna, M. Mazzotti, *Energy Environ. Sci.* **2022**, *15*, 3583–3602.
[8] A. Franco, C. J. S. Giovannini, *Sustainability* **2023**, *15*, 16917.
[9] S. Sun, C. Lv, W. Hong, X. Zhou, F. Wu, G. Chen, *ACS Appl. Energ. Mater.* **2019**, *2*, 312–319.
[10] S. Liu, H. Zhang, E. Hu, T. Zhu, C. Zhou, Y. Huang, M. Ling, X. Gao, Z. Lin, *J. Mater. Chem. A* **2021**, *9*, 23697–23702.
[11] Z. Chen, H. Yang, S. Mebs, H. Dau, M. Driess, Z. Wang, Z. Kang, P. W. Menezes, *Adv. Mater.* **2023**, *35*, e2208337.
[12] Giddaerappa, K. Naseem, K. Sharath, M. Mirabbos, K. S. Lokesh, *Electrochim. Acta.* **2024**, *475*, 143575.
[13] X. Ju, X. He, Y. Sun, Z. Cai, S. Sun, Y. Yao, Z. Li, J. Li, Y. Wang, Y. Ren, B. Ying, Y. Luo, D. Zheng, Q. Liu, L. Xie, T. Li, X. Sun, B. Tang, *iScience* **2024**, *27*, 108736.
[14] H. Jiang, H. Qin, P. Zhou, L. Kong, C. Wang, Z. Ji, X. Shen, G. Zhu, A. Yuan, *Int. J. Hydrogen Energy* **2024**, *58*, 892–901.
[15] H. Yang, P. V. Menezes, G. Dai, G. Vijaykumar, Z. Chen, M. Al-Shakran, T. Jacob, M. Driess, P. W. Menezes, *Appl. Catal. B* **2023**, *324*, 122249.
[16] H. Yang, G. Vijaykumar, Z. Chen, J. N. Hausmann, I. Mondal, S. Ghosh, V. C. J. Nicolaus, K. Laun, I. Zebger, M. Driess, P. W. Menezes, *Adv. Funct. Mater.* **2023**, *33*, 2303702.
[17] M. W. Louie, A. T. Bell, *J. Am. Chem. Soc.* **2013**, *135*, 12329–12337.
[18] D. Friebel, M. W. Louie, M. Bajdich, K. E. Sanwald, Y. Cai, A. M. Wise, M.-J. Cheng, D. Sokaras, T.-C. Weng, R. Alonso-Mori, R. C. Davis, J. R. Bargar, J. K. Nørskov, A. Nilsson, A. T. Bell, *J. Am. Chem. Soc.* **2015**, *137*, 1305–1313.
[19] M. S. Burke, M. G. Kast, L. Trotochaud, A. M. Smith, S. W. Boettcher, *J. Am. Chem. Soc.* **2015**, *137*, 3638–3648.
[20] C. Feng, F. Wang, Z. Liu, M. Nakabayashi, Y. Xiao, Q. Zeng, J. Fu, Q. Wu, C. Cui, Y. Han, N. Shibata, K. Domen, I. D. Sharp, Y. Li, *Nat. Commun.* **2021**, *12*, 5980.
[21] R. Chen, S. F. Hung, D. Zhou, J. Gao, C. Yang, H. Tao, H. B. Yang, L. Zhang, L. Zhang, Q. Xiong, H. M. Chen, B. Liu, *Adv. Mater.* **2019**, *31*, e1903909.
[22] H. Yang, M. Driess, P. W. Menezes, *Adv. Energy Mater.* **2021**, *11*, 2102074.
[23] D. Zhou, P. Li, X. Lin, A. McKinley, Y. Kuang, W. Liu, W. F. Lin, X. Sun, X. Duan, *Chem. Soc. Rev.* **2021**, *50*, 8790–8817.
[24] P. Wang, X. Zhang, B. Zhou, F. Meng, Y. Wang, G. Wen, *J. Environ. Chem. Eng.* **2023**, *11*, 111191.
[25] G. Huang, Y. Li, R. Chen, Z. Xiao, S. Du, Y. Huang, C. Xie, C. Dong, H. Yi, S. Wang, *Chin. J. Catal.* **2022**, *43*, 1101–1110.
[26] Q. Han, Y. Luo, J. Li, X. Du, S. Sun, Y. Wang, G. Liu, Z. Chen, *Appl. Catal. B* **2022**, *304*, 0926–3373.
[27] F. Hu, H. Wang, Y. Zhang, X. Shen, G. Zhang, Y. Pan, J. T. Miller, K. Wang, S. Zhu, X. Yang, C. Wang, X. Wu, Y. Xiong, Z. Peng, *Small.* **2019**, *15*, 1901020.
[28] B. M. Hunter, W. Hieringer, J. R. Winkler, H. B. Gray, A. M. Müller, *Energy Environ. Sci.* **2016**, *9*, 1734–1743.
[29] X. Xue, F. Yu, B. Peng, G. Wang, Y. Lv, L. Chen, Y. Yao, B. Dai, Y. Shi, X. Guo, *Sustain. Energy Fuels* **2019**, *3*, 237–244.
[30] X. Wang, R. Ma, S. Li, M. Xu, L. Liu, Y. Feng, T. Thomas, M. Yang, J. Wang, *Adv. Energy Mater.* **2023**, *13*, 2300765.
[31] J. N. Hausmann, P. W. Menezes, *Curr. Opin. Electrochem.* **2022**, *34*, 100991.
[32] K. Yu, H. Yang, H. Zhang, H. Huang, Z. Wang, Z. Kang, Y. Liu, P. W. Menezes, Z. Chen, *Nano-Micro Lett.* **2023**, *15*, 186.
[33] J. N. Hausmann, P. W. Menezes, *Angew. Chem. Int. Ed.* **2022**, *61*, e202207279.
[34] S. Li, R. Ma, J. Hu, Z. Li, L. Liu, X. Wang, Y. Lu, G. E. Sterbinsky, S. Liu, L. Zheng, J. Liu, D. Liu, J. Wang, *Nat. Commun.* **2022**, *13*, 2916.
[35] R. Zhang, L. Wang, L. Pan, Z. Chen, W. Jia, X. Zhang, J.-J. Zou, *Appl. Catal. B* **2020**, *277*, 119237.
[36] G. K. Schweitzer, L. L. Pesterfield, *The aqueous chemistry of the elements*, OUP USA, Oxford, **2010**.
[37] H. Lei, L. Ma, Q. Wan, S. Tan, B. Yang, Z. Wang, W. Mai, H. J. Fan, *Adv. Energy Mater.* **2022**, *12*, 2202522.
[38] H. Guo, L. Zhang, D. Ou, Q. Liu, Z. Wu, W. Yang, Z. Fang, Q. Shi, *Small* **2024**, *20*, 2307069.
[39] H. S. Jadhav, A. Roy, B. Z. Desalegan, J. G. Seo, *Sustain. Energy Fuels* **2020**, *4*, 312–323.
[40] Q. Kong, J. Wang, Z. Liu, S. Wu, X. Tong, N. Zong, B. Huang, R. Xu, L. Yang, *Dalton Trans.* **2023**, *52*, 16963–16973.
[41] X. Han, N. Li, J. S. Baik, P. Xiong, Y. Kang, Q. Dou, Q. Liu, J. Y. Lee, C. S. Kim, H. S. Park, *Adv. Funct. Mater.* **2023**, *33*, 2212233.
[42] H. Yang, J. N. Hausmann, V. Hlukhyy, T. Braun, K. Laun, I. Zebger, M. Driess, P. W. Menezes, *ChemCatChem* **2022**, *14*, e202200293.
[43] H. Yang, Z. Chen, W. Hao, H. Xu, Y. Guo, R. Wu, *Appl. Catal. B* **2019**, *252*, 214–221.
[44] Z. Gao, F. Liu, L. Wang, F. Luo, *Appl. Surf. Sci.* **2019**, *480*, 548–556.
[45] M. A. Oliver-Tolentino, J. Vázquez-Samperio, A. Manzo-Robledo, R. d. G. González-Huerta, J. L. Flores-Moreno, D. Ramírez-Rosales, A. Guzmán-Vargas, *J. Phys. Chem. C* **2014**, *118*, 22432–22438.
[46] J. N. Hausmann, P. V. Menezes, G. Vijaykumar, K. Laun, T. Diemant, I. Zebger, T. Jacob, M. Driess, P. W. Menezes, *Adv. Energy Mater.* **2022**, *12*, 2202098.
[47] S. Anantharaj, S. Noda, M. Driess, P. W. Menezes, *ACS Energy Lett.* **2021**, *6*, 1607–1611.
[48] J. N. Hausmann, S. Mebs, H. Dau, M. Driess, P. W. Menezes, *Adv. Mater.* **2022**, *34*, 2207494.
[49] P. W. Menezes, C. Walter, B. Chakraborty, J. N. Hausmann, I. Zaharieva, A. Frick, E. von Hauff, H. Dau, M. Driess, *Adv. Mater.* **2021**, *33*, 2004098.
[50] Q. Hong, Y. Wang, R. Wang, Z. Chen, H. Yang, K. Yu, Y. Liu, H. Huang, Z. Kang, P. W. Menezes, *Small* **2023**, *19*, 2206723.
[51] J. N. Hausmann, R. A. Khalaniya, C. Das, I. Remy-Speckmann, S. Berendts, A. V. Shevelkov, M. Driess, P. W. Menezes, *Chem. Commun.* **2021**, *57*, 2184–2187.

[52] H. Yang, G. Dai, Z. Chen, J. Wu, H. Huang, Y. Liu, M. Shao, Z. Kang, *Small* **2021**, *17*, 2101727.
[53] P. W. Menezes, S. Yao, R. Beltrán-Suito, J. N. Hausmann, P. V. Menezes, M. Driess, *Angew. Chem. Int. Ed.* **2021**, *60*, 4640–4647.
[54] H. Kaur, S. Bhatti, K. Singh, *J. Mater. Sci. Mater. Electron.* **2019**, *30*, 2246–2264.
[55] L. Trotochaud, S. L. Young, J. K. Ranney, S. W. Boettcher, *J. Am. Chem. Soc.* **2014**, *136*, 6744–6753.
[56] A. R. Blume, W. Calvet, A. Ghafari, T. Mayer, A. Knop-Gericke, R. Schlögl, *Phys. Chem. Chem. Phys.* **2023**, *25*, 25552–25565.
[57] T. J. Frankcombe, Y. Liu, *Chem. Mater.* **2023**, *35*, 5468–5474.
[58] J. N. Hausmann, S. Mebs, K. Laun, I. Zebger, H. Dau, P. W. Menezes, M. Driess, *Energy Environ. Sci.* **2020**, *13*, 3607–3619.
[59] H. Yang, J. Liu, Z. Chen, R. Wang, B. Fei, H. Liu, Y. Guo, R. Wu, *Chem. Eng. J.* **2021**, *420*, 127671.
[60] Y. Han, J. Wang, Y. Liu, T. Li, T. Wang, X. Li, X. Ye, G. Li, J. Li, W. Hu, Y. Deng, *Carbon Neutralization* **2024**, *3*, 172–198.
[61] H. Liao, G. Ni, P. Tan, K. Liu, X. Liu, H. Liu, K. Chen, X. Zheng, M. Liu, J. Pan, *Adv. Mater.* **2023**, *35*, 2300347.
[62] B. Yang, A. G. Tamirat, D. Bin, Y. Yao, H. Lu, Y. Xia, *Adv. Funct. Mater.* **2021**, *31*, 2104543.
[63] X. Wang, R. Ma, S. Li, M. Xu, L. Liu, Y. Feng, T. Thomas, M. Yang, J. Wang, *Adv. Energy Mater.* **2023**, *13*, 2300765.
[64] H. Liao, X. Zhang, S. Niu, P. Tan, K. Chen, Y. Liu, G. Wang, M. Liu, J. Pan, *Appl. Catal. B* **2022**, *307*, 121–150.
[65] F. Song, K. Schenk, X. Hu, *Energy Environ. Sci.* **2016**, *9*, 473–477.
[66] J. N. Hausmann, B. Traynor, R. J. Myers, M. Driess, P. W. Menezes, *ACS Energy Lett.* **2021**, *6*, 3567–3571.
[67] Z. Yu, Y. Duan, X. Feng, X. Yu, M. Gao, S. Yu, *Adv. Mater.* **2021**, *33*, 2007100.

Manuscript received: February 19, 2024
Revised manuscript received: April 16, 2024
Accepted manuscript online: April 21, 2024
Version of record online: July 22, 2024